npj | climate and atmospheric science

Article

Published in partnership with CECCR at King Abdulaziz University

https://doi.org/10.1038/s41612-025-01019-7

Oxygen-rich anionic metal silicate clusters as nucleation seeds for noctilucent clouds

Joan Mariñoso Guiu[1], Joost M. Bakker[2], Thorsten M. Bernhardt[3], John M. C. Plane[4], Stefan T. Bromley[1,5] & Sandra M. Lang[3]

Silicate-based meteoric smoke particles (MSPs) resulting from extraterrestrial dust impacting on the upper atmosphere are likely involved in seeding the formation of mesospheric ice-based noctilucent clouds (NLCs). However, the detailed physicochemical properties of MSP seeds remain elusive. Considering that ice formation is sensitive to MSP charging efficiency, here we focus on species which can efficiently capture charge. As in situ MSP characterisation is highly challenging, we mimic atmospheric MSP formation using laser ablation and collisional cooling to produce small anionic magnesium silicate clusters. Our detailed experimental and theoretical characterisation shows that these clusters have unusual oxygen-rich structures. Moreover, the corresponding neutral clusters have extraordinarily high adiabatic electron affinities and 3-18% charging efficiencies, which is remarkably consistent with estimates required by models to simulate atmospheric measurements. Overall, our highly oxidised anionic silicate clusters exhibit all necessary chemical, electronic and optical properties to be highly credible MSP-based seed candidates for NLC nucleation.

Noctilucent clouds (NLCs) are a spectacular high-altitude ice-based phenomenon with an earliest recorded observation in 1885[1]. NLCs are the highest clouds in Earth's atmosphere, occurring in the upper mesosphere (~82–85 km). This near space region interacts significantly with incoming radiation and cosmic dust, while also being sensitive to changes in the lower atmosphere. The increased availability of atmospheric water vapour due to the anthropogenic-induced increase in methane (which is oxidised to H_2O in the middle atmosphere), together with radiative cooling induced by increasing greenhouse gases, has been linked to increasing frequency and brightness of NLCs in recent decades[2–4]. The NLC ice mass is predicted to surge in the coming decades, which, due to the resulting increase in absorption of solar radiation, is likely to affect the photochemistry of the upper atmosphere[5]. For water vapour to condense into ice crystals, suitable seed particles are required[6]. The detailed nature of NLC condensation seeds is currently unknown, but they are widely thought to be nanosized meteoric smoke particles (MSPs)[7], that are derived from ablated cosmic dust particles[8–10]. As in situ characterisation of such species is extremely challenging[11], here we employ dedicated cluster beam experiments to mimic the MSP formation process. A systematic evaluation of the structures and properties of the formed clusters reveals that they appear to fulfil the criteria required to be compelling candidate NLC seeds.

The Earth's upper atmosphere is under continual bombardment with around 30 tonnes of dust particles entering the atmosphere every day[12,13]. These particles are typically silicate-rich with radii <250 μm, and enter at hyperthermal velocities so that ~30% of the incoming mass ablates between 80 and 105 km altitude[12]. The ablated atoms (mainly Si, Mg and Fe) cool through collisions with gas molecules and then undergo chemical reactions with O_3, O_2, H_2O and CO_2[14]. Subsequent aggregation of these species leads to the formation of MSPs. For MSPs to remain suspended above 80 km for more than a few hours against gravitational settling, they should be smaller than 2 nm in radius[15]. MSPs have been measured as heavy ions by sounding rocket payloads[16,17] and detected by incoherent scatter radar[18,19]; they are found to have a typical size range between 0.5 and 2 nm radius, in accordance with models[20,21]. The production of such MSPs is likely to be common to many planetary bodies which can hold an atmosphere (e.g. Venus, Mars, Titan, exoplanets)[21].

Incoming ionising solar radiation also leads to an abundance of free electrons in Earth's upper mesosphere (70–90 km). Below 85 km the electrons are typically depleted (by over 2 orders of magnitude) with respect to

[1]Departament de Ciència de Materials i Química Física & Institut de Química Teòrica i Computacional (IQTCUB), Universitat de Barcelona, Barcelona, Spain. [2]HFML-FELIX Laboratory, Institute of Molecules and Materials, Radboud University, Nijmegen, The Netherlands. [3]Institute of Surface Chemistry and Catalysis, Ulm University, Ulm, Germany. [4]School of Chemistry, University of Leeds, Leeds, UK. [5]Institució Catalana de Recerca i Estudis Avançats (ICREA), Barcelona, Spain. e-mail: s.bromley@ub.edu; sandra.lang@uni-ulm.de

positive ions, due to their capture by strongly electronegative species[20,22]. MSPs are a potential electron sink and, indeed, negatively-charged MSPs have been detected using Faraday cups on sounding rocket payloads[20,23–25]. The charging of MSPs would help these small species to overcome the Kelvin effect[26] (i.e., increased vapour pressure for particles with a small radius), making them more effective nucleation seeds. Such MSPs have been proposed as providing recombination sites for O and H_2 to explain the unexpected presence of water vapour in the mesosphere[27]. Based on detection data, models estimate that around 6% of all MSPs need to be charged at an altitude between 80 and 90 km, where the plasma and MSP densities are similar[22]. This implies that some MSPs have very high electron attachment rates while being resistant to various electron detachment processes.

To mimic the ablation and recondensation formation processes of negatively charged MSPs in a controlled laboratory setting, we use laser ablation of a Si/Mg surface to produce thermally excited atomic/ionic species which we react with a low concentration of gaseous oxygen, all the while collisionally cooling them with helium to form small negatively charged $Mg_xSi_yO_z^-$ clusters. We identify the structures of a range of size-selected $Mg_xSi_yO_z^-$ clusters by comparing experimental infrared multiple photon dissociation (IR-MPD) spectra with those from accurate quantum chemical calculations for candidate structures. Our formed $Mg_xSi_yO_z^-$ species are found to be unexpectedly oxygen-rich (i.e. $z > 2(x + y)$), where some oxygen is present as superoxo-like O_2 or ozone-like O_3 molecules as well as oxygen radicals. Our analysis reveals that the electron affinities (EAs) of the corresponding neutral 'over-oxidised' $Mg_xSi_yO_z$ clusters are extremely high (typically >4.2 eV), indicating an oxidation-induced increase in electronic stability. Based on kinetic considerations of electron attachment/detachment rates, we also show that these high-EA species have a charging efficiency of 3–18%, in good agreement with average values needed by models to simulate atmospheric measurements. Overall, these small, highly oxidised magnesium silicate clusters are thus highly credible candidate NLC nucleation seeds. Incorporation of the properties of such species in atmospheric/climate models should lead to an improved understanding of the chemistry of the upper atmosphere and help clarify the link between NLC formation and climate change.

Results

IR-MPD spectra of negatively charged $Mg_xSi_yO_z^-$ clusters

Anionic magnesium silicate clusters were produced by pulsed laser ablation of a binary Mg_2Si target in the presence of a 1% O_2/He gas mixture and subsequently studied by IR-MPD spectroscopy, quantified in spectra as the depletion yield as a function of wavenumber (see Section S1 of the Supporting Information (SI)). In the following we present in detail the spectrum of $MgSiO_6^-$ as the simplest system by comparing it with calculated spectra of several isomeric structures, and subsequently evaluate structure growth by considering spectra of $MgSi_2O_8^-$ (SiO_2 added), $MgSi_2O_7^-$ (+SiO), $Mg_2SiO_6^-$ (+Mg), and $Mg_2SiO_7^-$ (+MgO) (Fig. 1). Spectra with isotopically labelled ^{18}O, vibrational mode assignment and further isomeric structures can be found in section S2 of the SI.

The IR-MPD spectrum of $MgSiO_6^-$ shows seven bands (labelled I-VII) in the 225–1400 cm^{-1} spectral region. The lack of any bands above 1400 cm^{-1} (Figure S6 of the SI) already indicates a rather strong binding of all oxygen (the vibrational frequency of free oxygen molecules is 1580 cm^{-1}) and the absence of any loosely bound O_2 units. This sharply contrasts with what was previously observed for highly oxidised magnesium silicate cluster cations[28]. The calculated lowest energy isomer of $MgSiO_6^-$ (isomer 1,1,6-a in Fig. 1) consists of a $MgSiO_2^-$ monomer with two superoxide-like O_2 units (total charge ~−0.5 |e|). The computed spectrum does not fully agree with the experimental one; specifically, the strong predicted band at ~1100 cm^{-1} (Si-O_2 stretching vibration) is not observed in the experiment and the experimental band I is not reproduced by the calculations. However, a

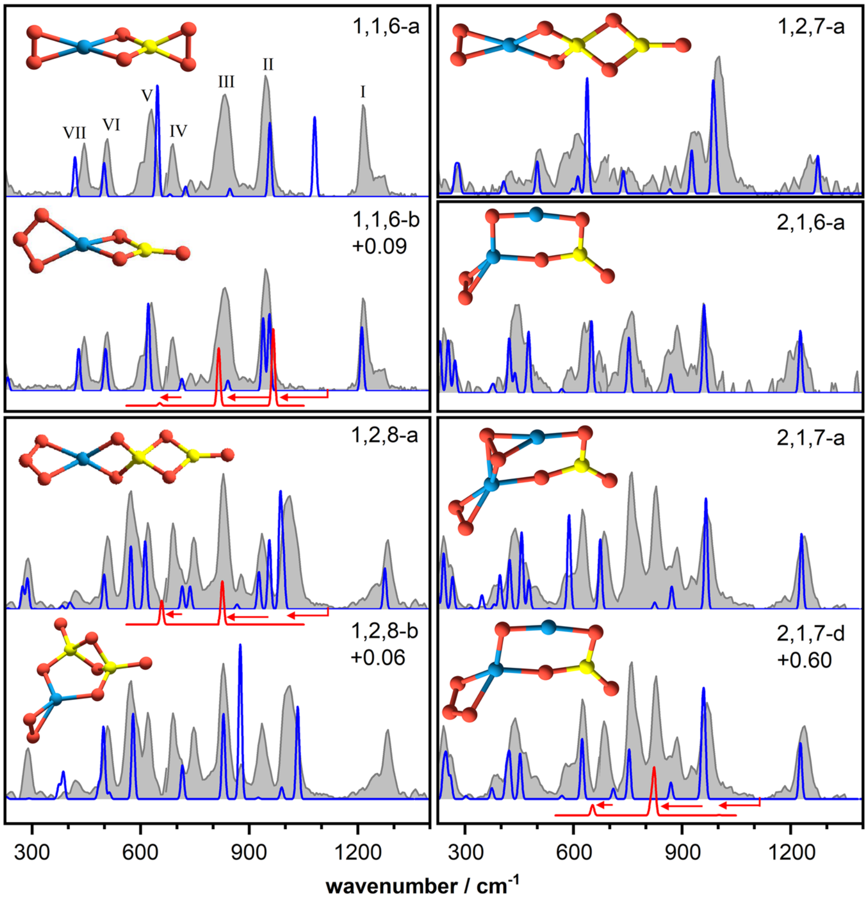

Fig. 1 | Experimental IR-MPD spectra (in grey) of various $Mg_xSi_yO_z^-$ together with the DFT-calculated spectra (in blue; PBE0 functional, relative energies in eV) of the lowest energy isomers. The red curves represent the O_3 modes of the shown structures obtained with the PBE functional. The IR-MPD spectra were measured in two independent runs and are the average of five (650–1800 cm^{-1}) and six (225–700 cm^{-1}) individual spectra, respectively, and a 3-point adjacent average of the individual data points. To achieve intensity match of the two spectra, the experimental spectrum in the high wavenumber range was multiplied with a factor of 3.9. The chosen naming $x,y,z - n$ denotes the elemental composition of $Mg_xSi_yO_z$ and $n = a,b,c$ indicates the isomer sorted in order of increasing energy (further isomers can be found in section S2 of the SI). Mg, Si, and O atoms are depicted as blue, yellow, and red spheres, respectively.

second almost isoenergetic isomer (1,1,6-b) was found, consisting of a $MgSiO_3^-$ monomer with a terminally bound oxygen radical and an ozone-like O_3 unit. This structure is similar to the recently found structure of the cationic $MgSiO_9^+$, but with the O_3 unit attached to the Mg rather than the Si atom[28]. The predicted vibrational spectrum of 1,1-6-b accounts for all seven experimentally observed bands, although the intensity of bands III (SiO_3 symmetric stretch) and IV (O_3 bending) are underestimated by the calculations and the frequency of the latter is predicted to be ~30 cm^{-1} too high. This intensity mismatch suggests a rather poor treatment of the O_3 unit by the PBE0 functional (similar to weakly bound O_2 units as recently observed for cationic clusters[28]), while MgO and SiO modes are very accurately described. Indeed, a considerably improved match between the experimental and theoretical spectra can be achieved when calculating the O_3 modes with the PBE functional (red curve; since the PBE functional only improves the description of the O_3 bands but worsens the MgO and SiO modes, we restrict the red curve to the relevant O_3 modes): the intensity of the O_3 symmetric stretching vibration increases and the mode shifts from 1192 cm^{-1} (very low intensity with PBE0) to 966 cm^{-1} and, most importantly, the O_3 asymmetric stretching vibration shifts from 956 cm^{-1} to 816 cm^{-1} leading to a very good match with band III. A minor dissonant is that the O_3 bending vibration, a match for band IV, maybe shifts too much with PBE (714 cm^{-1} vs. 653 cm^{-1} with PBE0). The potential formation of isomer 1,1,6-b is further strengthened by the spectra obtained with isotopically enriched oxygen, $MgSi^{18}O_6^-$ (Fig. S7 of the SI). A possible explanation for the favoured formation of isomer 1,1,6-b is the preferential formation of $MgSiO_3^-$ monomer with respect to $MgSiO_2^-$. This scenario is supported by the large binding energy of an O atom to the $MgSiO_2^-$ monomer (~8 eV). Therefore, this formation path would likely prevent the formation of isomer 1,1,6-a, leading to the observed predominance of isomer 1,1,6-b. We also note that the predicted very small energy difference between 1,1,6-a and 1,1,6-b is likely to be within the error of the theoretical calculations.

Adding a SiO_2 and SiO unit, respectively, to $MgSiO_6^-$ leads to chain-like structures consisting of a $MgSiO_2$ and a Si_2O_2 ring. In the case of $MgSi_2O_8^-$ the terminal oxygen radical and the O_3 unit are retained (isomer 1,2,8-a), whereas in the case of $MgSi_2O_7^-$ the O_3 unit is replaced by a superoxo-like O_2 unit (isomer 1,2,7-a). The calculated vibrational spectrum of 1,2,8-a can explain all of the experimentally observed features, especially with the O_3 modes recalculated with the PBE functional (red curve). A second almost isoenergetic isomer 1,2,8-b with a more compact structure clearly fails to explain the IR-MPD spectrum. The disappearance of O_3 in isomer 1,2,7-a is in agreement with the absence of the intense band around 830 cm^{-1} (band III for $MgSiO_6^-$). Instead, the superoxo-like O_2 (total charge ~−0.5 |e|, d(O-O) = 1.33 Å) results in an O-O stretching mode at 1194 cm^{-1}, which, however, has such a low intensity that it cannot be seen in the vibrational spectrum. All other predicted modes are in favourable agreement with the IR-MPD spectrum and can account for all experimentally observed bands, as well as in the isotopically labelled experiments (Fig. S9 of the SI).

Next, we investigated the structural evaluation of the magnesium silicate clusters by addition of an Mg atom or an MgO unit. The lowest energy structure of $Mg_2SiO_6^-$ (isomer 2,1,6-a) consists of a six-membered Mg_2SiO_3-ring with a terminal oxygen atom and a superoxide-like O_2 (total charge ~−0.5 |e|) bound to one of the Mg atoms, similar to the previously predicted neutral olivine monomer Mg_2SiO_4[29]. This structure predicts extremely well all features of the IR-MPD spectrum, with confirmation found in the spectra of the isotopically labelled $Mg_2Si^{18}O_6^-$ (Fig. S10 of the SI). Addition of a further oxygen atom, yielding $Mg_2SiO_7^-$, leads to some distortion of the six-membered Mg_2SiO_3 ring due to the bridge-binding of this oxygen atom (isomer 2,1,7-a; d(O-O) = 1.54 Å, O-O stretching at 824 cm^{-1}). This isomer can account for most of the experimentally observed features but clearly fails to explain the two intense bands around 760 cm^{-1} and 825 cm^{-1}. However, we found a higher energy (+0.60 eV) isomer 2,1,7-d (the somewhat lower energy isomers 2,1,7-b,c shown in Figure S11 of the SI do not match the spectrum) that is formed from 2,1,6-a by replacing the superoxo-like O_2 with an ozone-like O_3; this isomer is in excellent agreement with the experimental spectrum when the O_3 modes are calculated with the PBE functional. Although the co-existence of 2,1,7-a in the molecular beam cannot be excluded based on the vibrational spectrum, the high intensity of the 760 cm^{-1} band (which stems from the loss of >90% of all $Mg_2SiO_7^-$ clusters when irradiating at this frequency) indicates that 2,1,7-d is the only isomer present in the experiment. This leads us to speculate that 2,1,7-d is preferably formed and interconversion into the lower energy structure 2,1,7-a is hindered. This observation is in line with previous studies of anionic bare and deuterated silicon clusters and titanium oxide clusters[30,31], where high vertical EAs of neutral clusters determine the observed anions, rather than the energetic stability of the anions. This was rationalised by a cluster formation mechanism starting with neutral species, followed by electron attachment from the plasma created in a pulsed arc or laser vaporisation source, respectively, and which favours isomers with high vertical EAs. If the interconversion into lower energy isomers is kinetically hindered, the clusters only relax to metastable structures on the time scale of the experiment. The isomers experimentally observed in the present study are the ones with the highest vertical EAs (1,1,6-b, 1,2,8-a, and 2,1,7-d), as will be discussed below (cf. Table 1), although other isomers are energetically more stable or (almost) isoenergetic.

Table 1 | Computed vertical and adiabatic electron affinities (EAs) of some $Mg_xSi_yO_z$ clusters representing the neutral analogues to the anionic structures identified via IR-MPD spectroscopy and DFT calculations as well as their energetically low-lying isomers

Species	EA (vertical)	EA (adiabatic)	Reference
$MgSiO_6$ (1,1,6-a)	3.53	4.55	This work
$MgSiO_6$ (1,1,6-b)	4.35	4.82	This work
$MgSi_2O_7$ (1,2,7-a)	3.51	5.23	This work
$MgSi_2O_8$ (1,2,8-a)	4.03	5.20	This work
$MgSi_2O_8$ (1,2,8-b)	3.66	4.88	This work
Mg_2SiO_6 (2,1,6-a)	3.96	4.48	This work
Mg_2SiO_7 (2,1,7-a)	2.27	4.22	This work
Mg_2SiO_7 (2,1,7-b)	3.78	5.21	This work
Mg_2SiO_7 (2,1,7-d)	3.75	4.44	This work
$FeSi_2O_7$	3.01	4.68	This work
Cl	4.58	4.58	This work
NO_3	3.66	3.86	This work
HCO_3	2.80	3.45	This work
$(MgO)_n$		0.70–1.62	Ref. 33
Si_xO_y	0–3.75	0.46–2.6	Refs. 34–37
olivine $(Mg_2SiO_4)_n$	0.6–1.1	1.98–2.65	Refs. 20,37
pyroxene $(MgSiO_3)_n$	0.7–1.9	1.59–2.83	Refs. 20,37

The structures of the neutral clusters (cf. Fig. S12) are very similar to the anionic analogues, with the exception of 2,1,7-a that shows some structural rearrangements upon removing the extra electron. For comparison EAs are also given of some highly electronegative species in the mesosphere (Cl, NO_3, HCO_3), the MgO-, SiO- and MgSiO-clusters reported in the literature, as well as the iron-containing $FeSi_2O_7$. All values are in eV.

In summary, comparison of the experimental IR-MPD spectrum with the calculated vibrational spectra of several isomers leads us to conclude that $MgSiO_6^-$ consists of a pyroxene monomer and an ozone-like species, $(MgSiO_3)O_3^-$. Addition of a SiO_2 or SiO unit yields chain-like structures containing four-membered $MgSiO_2$ and Si_2O_2 rings, while addition of Mg or MgO yields six-membered Mg_2SiO_3 ring. All clusters contain terminally bound oxygen radicals and tend to form ozone-like O_3 units when sufficient oxygen is present. Only when the clusters lack one oxygen atom, the O_3 unit is replaced by a superoxo-like O_2.

Table 2 | Rate coefficients and reaction enthalpies for various reaction processes (rows 2–6) and resulting fraction of anionic clusters with respect to neutral clusters (row 7)

Reaction		$MgSi_2O_7$ (isomer a)	Mg_2SiO_7 (isomer a)	Mg_2SiO_7 (isomer b)	$FeSi_2O_7$
$Mt_xSi_yO_z + e^- \rightarrow Mt_xSi_yO_z^-$	k_{ea} [(a)]	$2.18 \times 10^{-6} (T/200)^{-0.610}$	$1.49 \times 10^{-6}(T/200)^{-0.577}$	$1.02 \times 10^{-6}(T/200)^{-0.524}$	$1.58 \times 10^{-6}(T/200)^{0.578}$
$Mt_xSi_yO_z^- + O \rightarrow Mt_xSi_yO_{z+1} + e^-$	ΔH^0 [(b)]	2.56	0.69	0.51	1.60
$Mt_xSi_yO_z^- + O \rightarrow Mt_xSi_yO_{z+1} + e^-$	ΔH^0 [(c)]	3.01	1.13	0.96	2.07
$Mt_xSi_yO_z^- + h\nu \rightarrow Mt_xSi_yO_z + e^-$	k_{pd} [(d)]	6.6×10^{-4}	1.4×10^{-3}	2.0×10^{-3}	3.4×10^{-3}
$Mt_xSi_yO_z^- + I^+ \rightarrow Mt_xSi_yO_z + I$	k_{nr} [(a)]	3.8×10^{-8}	3.1×10^{-8}	2.4×10^{-8}	3.3×10^{-8}
$\frac{[Mt_xSi_yO_z^-]}{[Mt_xSi_yO_z]} = \frac{k_{ea}[e^-]}{k_{pd} + k_{nr}[I^+]}$	(e)	0.16	0.05	0.03	0.02

[a] Bimolecular reactions in units cm^3 $molecule^{-1}$ s^{-1}.

[b] Enthalpy in eV at 0 K.

[c] Enthalpy in eV at 220 K and the typical pressure in the mesosphere of 10^{-5} bar.

[d] Unimolecular reaction in units s^{-1}, obtained by using adiabatic electron affinities;

[e] $[I^+]$ is the total plasma density.

Mt = Mg or Fe.

Atmospheric relevance

Although the number densities and reaction time scales in the present experiment and in the atmosphere are different, the formation mechanisms are likely not dissimilar with the helium adopting the role of coolant that air molecules have in the atmosphere, ensuring near-thermal equilibrium and dissipating excess energy in between the sequential adsorption steps in the growth process. Evidence for this 'cold' chemistry was found, for instance, in the structure determination of pure copper clusters, where each cluster of *n* atoms was shown to retain the structure of the cluster with one atom less[32]. Even in the case of isomer 2,1,7, where we do not observe the thermodynamic minimum, the formation of the neutral thermodynamic minimum, followed by electron attachment appears a fully plausible growth scenario in the upper atmosphere.

Measurements with rocket-borne particle detectors have revealed the existence of negatively charged MSPs with typical radii ranging between 0.5 and 2 nm in the upper mesosphere[16,17,20]. Of particular interest is the fraction of MSPs that are charged in this region where the plasma density and MSP density are similar. Models of dust plasmas predict that only around 6% of MSPs are charged between 80 and 90 km, so that the total MSP concentration—which is the important geophysical quantity—has to be estimated by multiplying the number measured by a significant factor (~16)[20]. However, these models are sensitive to the MSP charging efficiency, which is poorly understood. To address this problem, we use the above studied anionic magnesium silicate clusters, which represent appropriate analogues for MSPs with respect to both size and elemental composition, to study their charging efficiency under conditions of the upper mesosphere by kinetic modelling of electron attachment to neutral clusters as well as of potential competing processes leading to subsequent cluster destruction.

The neutral analogues to the anionic structures identified via IR-MPD spectroscopy and DFT calculations, as well as their energetically low-lying isomers (<0.3 eV of the respective minimum energy structures), all have very high adiabatic electron affinities (EAs) ranging between 4.22 and 5.21 eV. These EAs are not only considerably higher than the EAs of electronegative species in the mesosphere such as Cl, NO_3, HCO_3 (cf. Table 1), but also than the EAs of magnesium oxide clusters[33], stoichiometric and oxygen-rich silicon oxide clusters[34–36], and stoichiometric olivine- (Mg_2SiO_4) and pyroxene-like ($MgSiO_3$) silicate clusters[20,37]. We attribute the extremely high EAs of the clusters found herein to the high oxidation leading to superoxo- and ozone-like ligands. We note that the adiabatic EA relates to the energy difference between the optimised ground state geometry of a neutral species and its anion after full relaxation. Unlike the vertical EAs (also provided in Table 1) where no relaxation is considered, adiabatic EAs better represent the thermodynamics of electron capture and are more relevant for chemical and physical processes where relaxation can occur.

For calculating the charging efficiency, three clusters were chosen as model systems: $MgSi_2O_7$ (isomer 1,2,7-a) and Mg_2SiO_7 (isomer 2,1,7-b), the two clusters with the highest EAs, and Mg_2SiO_7 (isomer 2,1,7-a), the cluster with the lowest EA (Table 1). For comparison we have also calculated the charging efficiency for $FeSi_2O_7$ to evaluate the potential role of iron, which is likely present in MSPs. The necessary physical parameters for the anionic and neutral clusters were obtained by DFT calculations (Table 1 and S6–S8). The rate constants for electron attachment k_{ea} calculated by RRKM theory are very large and close to the Langevin high-pressure-limits k_L at the pressure of the upper mesosphere (10^{-5}bar)[20] (see Eq. 1 in the Methods section and Table 2). These large rate coefficients can be attributed to the high densities of the rovibrational states, in turn caused by both the large EAs and the rather large number of low-frequency vibrational modes (see Table S7), as well as their sizable polarizabilities and dipole moments (see Table S6). It is interesting to compare these rate coefficients with the expression from Natanson[38] (k_{ea}^{Nat}, Eq. 2). For k_{ea}^{Nat} to equal k_{ea}, the particle radius r_{MSP} would need to be 0.70, 0.57 and 0.45 nm for $MgSi_2O_7$ (isomer a), Mg_2SiO_7 (isomer a) and Mg_2SiO_7 (isomer b), respectively. These values are somewhat larger than the effective geometric radii of these molecules amounting to ~0.42 nm for $MgSi_2O_7$, and ~0.30 nm for both Mg_2SiO_7 isomers, which is consistent with the significant long-range forces caused by the large dipole moments and polarizabilities of the Mg-silicate molecules. Note that dissociative electron attachment could also occur, e.g. $Mg_2SiO_7 + e^- \rightarrow Mg_2SiO_5^- + O_2$ is exothermic. However, if this did occur, $Mg_2SiO_5^-$ would rapidly recombine with atmospheric O_2 to yield $Mg_2SiO_7^-$. Moreover, the rate of electron attachment is already essentially at the high-pressure limit in the upper mesosphere, and dissociative electron attachment would also be governed by the same long-range capture rate.

Once the anionic clusters have formed, they can potentially be destroyed by several processes: associative detachment with atomic oxygen, photodetachment, or via a neutralisation reaction with a positive ion I^+ (see Table 2). Among these, associative detachment with atomic O, which has a high concentration in the upper mesosphere[14], is calculated to be endothermic (see Table 2) for all of the studied clusters both at 0 and 220 K and thus not a likely process at low temperatures 220 K). We note that the reverse reactions are exothermic and correspond to dissociative electron attachment reactions, which can also produce Mg-silicate anions. To estimate the rate constant k_{pd} for photodetachment—which could occur during daytime—the absorption cross sections were calculated as a function of wavelength as shown in Fig. 2. Due to the large EAs, the thresholds for photodetachment lie at unusually low wavelengths in the near UV. Convolving these cross sections up to their respective thresholds with the solar actinic flux (averaged over a solar cycle) from the semi-empirical SOLAR2000 model[39] gives very low photodetachment rates, k_{pd}, on the order of $10^{-4} - 10^{-3}\,s^{-1}$ (Table 2; for comparison a value of 0.3 s^{-1} was obtained for O_2^-[40]).

Finally, rate constants for the reaction with positive ions were calculated using the expression derived by Natanson[38] under assumption of a

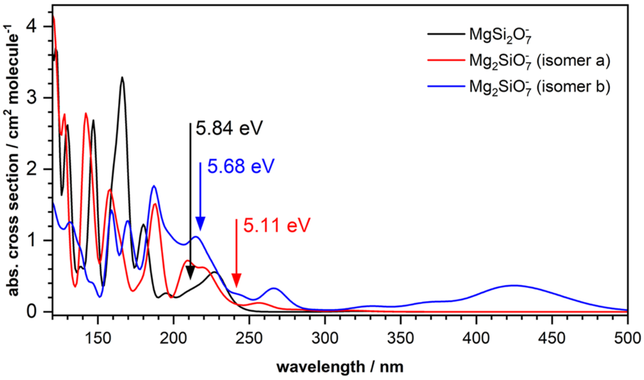

Fig. 2 | Calculated absorption cross sections for anionic $MgSi_2O_7^-$ (isomer 1,1,7-a; black curve), $Mg_2SiO_7^-$ (isomer 2,1,7-a; red curve) and $Mg_2SiO_7^-$ (isomer 2,1,7-b; blue curve) as a function of the wavelength. The arrows indicate the electron photodetachment thresholds calculated as the energy difference between the anionic and neutral clusters, both in their relaxed geometries.

mean positive ion mass of 100 amu and the above estimated r_{MSP}. At a temperature of 200 K the rate constants k_{nr} are on the order of $(2.4–3.8) \times 10^{-8}$ cm^3 mol^{-1} s^{-1} (see Table 2). Considering all of these processes the fraction of charged particles can be calculated. Under assumption of an electron density of 50 cm^{-3} at 80 km height (a typical plasma density at this height is 1000 cm^{-3}, with an electron density that is ~5% of this[20,24,41]) the fraction is 0.18 for $MgSiO_7^-$, 0.05 for $Mg_2SiO_7^-$ isomer a, as well as 0.03 for isomer b. It should be noted that replacing Mg by Fe does not notably change the EA, rate constants, and charging efficiency, validating our model of magnesium silicate particles.

Considering the uncertainties and assumptions in the dust plasma models used to estimate the 0.06 charged fraction, our values 0.03-0.18 based on accurate calculation of the properties of well-characterised experimental anionic MSP analogues are consistent with current estimates, which validates the view that the negative heavy ions measured by rocket-borne payloads and radar are a small fraction of the total MSP population[24,42,43]. Overall, this systematic analysis shows that the properties of our oxygen-rich MSP analogues comply with all the necessary criteria for being viable nucleation seeds for NLCs.

Discussion

In summary, we produced anionic magnesium silicate clusters by laser ablation of a solid Si/Mg precursor material in the presence of a He gas with low O_2 concentration, mimicking the ablation and recondensation process of negatively charged silicate MSPs in the upper mesosphere. Subsequent characterisation of the formed species via a combination of mass spectrometry, IR-MPD spectroscopy, and quantum-chemical calculations revealed the preferred formation of oxygen rich clusters ($Mg_xSi_yO_z^-$ with $z > 2(x + y)$) in which some oxygen is bound as oxygen radicals, superoxo-like O_2 and/or ozone-like O_3 units to four- and six-membered MgSiO rings. Furthermore, we show that the corresponding neutral counterparts have extraordinarily high adiabatic electron affinities (>4.2 eV), a necessary prerequisite for their formation and survival in the upper mesosphere. Indeed, kinetic modelling of electron attachment to the highly oxidised neutral clusters in competition with various anion destruction processes reveals a significant charging efficiency of 3–18%, depending on the exact cluster size and composition. To match mesospheric observations, simulations require that the average charging efficiency should be around 6%. The good agreement between these independently obtained values underlines the potential atmospheric relevance of our clusters

The main overall finding our work is that highly oxidised anionic silicate clusters exhibit all the necessary chemical, electronic and optical properties to be highly credible candidates for MSP-based NLC nucleation seeds in the upper mesosphere. Our study thus provides fundamental new insights into the potential nature and properties of MSPs and could help towards providing a molecular-level understanding of MSP charging efficiency. In addition to these physicochemical results, incorporation of our results into atmospheric/climate models should also lead to an improved understanding of NLC formation and the wider chemistry of MSPs in the upper mesosphere.

Methods

Experimental methods

Anionic magnesium silicate clusters were produced by pulsed laser ablation of a rotating MgSi rod target (Mg:Si = 2:1 molar ratio) using the second harmonic of a Nd:YAG laser (532 nm). The ablation took place in a 3 mm diameter and 60 mm long growth channel in the presence of a short pulse of helium carrier gas seeded with 1% oxygen. The gas mixture was then expanded into vacuum forming a molecular beam, which was shaped by a 2 mm diameter skimmer and a 0.45 mm slit aperture, before entering the intracavity region where it interacted with the IR laser beam of the Free Electron Laser for Intra Cavity Experiments (FELICE, 225−1800 cm^{-1}; a 10 µs macropulse with picosecond duration micropulses at 1 GHz repetition rate; spectral width set to ~0.5% FWHM of the central wavenumber) crossing it at an angle of 35°. A few microseconds after interaction with FELICE, all ions were extracted by a set of pulsed high-voltage plates into a reflectron time-of-flight mass spectrometer and detected with a micro-channel plate detector[44,45]. To correct for long-term source fluctuations, the experiment was operated at twice the FELICE repetition rate, allowing for the recording of reference mass spectra in between successive FELICE pulses.

Whenever the IR frequency was in resonance with an IR-active vibrational mode of a given complex, multiple IR photons were absorbed sequentially, leading to a heating of the complex and finally to its fragmentation, and consequently to a depletion of the detected signal in the mass channel of the complex. The IR-MPD spectra shown in this contribution represent the depletion yield $Y(\tilde{\nu})$ at wavenumber $\tilde{\nu}$, obtained via the equation $Y(\tilde{\nu}) = -ln\,[I(\tilde{\nu})/I_0]/P(\tilde{\nu})$ where $I(\tilde{\nu})$ and I_0 are the mass peak intensities with and without laser light, respectively, and $P(\tilde{\nu})$ is the macropulse energy. In the linear absorption approximation, the absorption probability is the product of IR absorption cross section and photon flux. In reconstructing the photon flux from the macropulse energy, the wavelength dependence of the beam geometry and of the photon energy cancel out, but the dependence of spectral bandwidth on wavelength must be corrected for. Therefore, to obtain a more faithful comparison between experimental and calculated band intensities, the latter are divided by the wavenumber.

Computational methods

In our initial searches for stable anionic magnesium silicate clusters, we assumed that the experimentally obtained clusters consisted of an anionic silicate core interacting in a non-bonded fashion with oxygen molecules. Following this idea, we obtained low-energy candidates for the anionic cores using the Monte Carlo basin hopping algorithm[46] (MCBH) in combination with a polarisable classical interatomic potential (IP)[47]. This approach has previously been shown to be effective in finding low-energy silicate cluster isomers[29]. Once the low-energy cluster core structures were obtained, we systematically sampled different positions for the surrounding oxygen molecules. The General Utility Lattice Programme (GULP)[48] was used to perform the IP-based local optimisations needed during the MCBH searches.

In addition to our IP-based searches, we also used Global Optimisation with First-principles Energy Expression (GOFEE)[49] searches to obtain low-energy cluster candidates. GOFEE uses single-point calculations to widely sample the potential energy landscape of cluster configurations while dynamically training a surrogate machine learning energy model. We performed this sampling using Density Functional Theory (DFT) based calculations. Using the surrogate model, GOFEE can efficiently evaluate forces and perform energy minimisations with an accuracy approaching the level of the single-point DFT sampling. The DFT calculations employed the PBE0 hybrid exchange-correlation functional[50] and a light-tier 1 numerical atom-centred orbital basis set[51]. Although computationally more expensive than our IP-based searches, the GOFEE approach does not depend on a specific IP parameterisation.

The structures of all obtained cluster candidates from both sets of searches were reoptimized using DFT-based calculations using the PBE0 functional and a tight-tier 2 numerical atom-centred orbital basis set[52]. We note that PBE0-based DFT calculations have been shown to be accurate for computing the energetics of small oxide clusters interacting with oxygen molecules, with respect to renormalized second-order perturbation theory calculations[53]. Non-bonded dispersive interactions were also considered using the Tkatchenko-Scheffler method[54]. All DFT-based calculations were carried out using the Fritz Haber Institute Ab Initio Molecular Simulations package (FHI-AIMS)[52].

For the 5–10 lowest energy cluster isomers found for each composition, we also used the PBE0/tight-tier 2 level of DFT theory to calculate their harmonic IR spectra. Previous studies have shown that DFT calculations using PBE0 provide accurate IR spectra but tend to systematically slightly overestimate the computed frequency values when compared with accurate theoretical data for pyroxenic and olivinic neutral monomers[55], and experimental values for cationic nanosilicates[28], and bulk crystalline olivinic[56] and pyroxenic[57] materials. To compensate for this effect, we apply a constant 3% redshift (i.e. a 0.97 scaling factor) to all our calculated frequencies. Additionally, for a better visual comparison with the experimentally obtained spectra, we broadened each computationally obtained signal by convolving it with a Gaussian lineshape function with a full width at half maximum of 20 cm^{-1}. For specific vibrations involving bound O_3 moieties, DFT calculations using the PBE functional[58] were employed to correct the known deficiencies of using the PBE0 functional for such cases (e.g. ozone[59]).

Adiabatic EAs were calculated as the energy difference between the optimised structures of the neutrals and anions. The structures of the neutral clusters were obtained by DFT-based (PBE0/tight-tier 2) relaxation of the anionic structures with one electron less. Vertical electron affinities (EA) were calculated from the energy difference between the optimised neutral cluster structure and the anion at the same geometry. We note that the vertical electron detachment energy (VDE) relates to the opposite process (i.e. the energy required to remove an electron from an anion to form a neutral species, assuming that the geometry of the anion remains unchanged).

Determination of rate constants

The rate coefficients for electron attachment to these molecules were calculated using Rice-Ramsperger-Kassel-Markus (RRKM) theory with an inverse Laplace transform solution of the Master Eq.[60]. Electron attachment occurs through formation of an excited adduct anion; this can either dissociate again to the neutral and an electron, be stabilised by collision with a third body (which is N_2 or O_2 in the mesosphere/lower thermosphere), or dissociate to anion and neutral products i.e. dissociative attachment (which we do not include in the RRKM calculation). For these reactions, the internal energy of the adduct was divided into a contiguous set of grains (width 60 cm^{-1}), each containing a bundle of rovibrational states. Each grain was then assigned a microcanonical rate coefficient for dissociation, using inverse Laplace transformation[20] to link directly to the high pressure-limiting of the electron-molecule recombination rate coefficient k_L given by modified Langevin theory according to:

$$k_L = 2\pi e\chi\sqrt{\frac{\alpha}{4\pi\epsilon_0\mu}}. \tag{1}$$

where α is the volume polarizability of the Mg-silicate, e is the electronic charge, ϵ_0 is the vacuum permittivity, μ is the reduced mass of the e^- - silicate collision pair and χ is a correction for s-wave scattering[61]. Due to the large dipole moments (particularly for $MgSi_2O_7$), the calculated Langevin rate is increased compared to Eq. (1) using the parameterisation from Su and Chesnavich for polar molecules[62].

The density of states of the adduct was calculated using the Beyer–Swinehart algorithm for the vibrational modes (without correcting for anharmonicity), and a classical densities of states treatment for the rotational modes. The vibrational frequencies and rotational constants for the three Mg-silicate molecules and their respective anions are given in Tables S7 and S8 of the SI. For comparison, rate constants were also calculated using the expression from Natanson[38]:

$$k_{ea}^{Nat} = \pi r_{MSP}^2\sqrt{\frac{8k_BT}{\pi m_e}}\cdot\left(1+\sqrt{\frac{e^2}{8\epsilon_0\, r_{MSP}k_BT}}\right) \tag{2}$$

where k_B is the Boltzmann constant, m_e is the mass of an electron, and r_{MSP} the radius of the particle.

Data availability

The following data is available in the Supporting Information: (i) assignment of mass peaks, (ii) IR-MPD spectra of $Mg_xSi_y{}^{16}O_z{}^-$ and $Mg_xSi_y{}^{18}O_z{}^-$, (iii) calculated spectra for further isomers, (iv) calculated properties of selected neutral and anionic clusters.

Received: 18 December 2024; Accepted: 22 March 2025;

References

1. Gadsden, M., Schröder, W. *Noctilucent Clouds* (Springer, 1989).
2. Thomas, G. E., Olivero, J. J., Jensen, E. J., Schroeder, W. & Toon, O. B. Relation between increasing methane and the presence of ice clouds at the mesopause. *Nature* **338**, 490–492 (1989).
3. Thomas, G. E. & Olivero, J. Noctilucent clouds as possible indicators of global change in the mesosphere. *Adv. Space Res.* **28**, 937–946 (2001).
4. Lübken, F.-J., Berger, U. & Baumgarten, G. On the anthropogenic impact on long-term evolution of noctilucent clouds. *Geophys. Res. Lett.* **45**, 6681–6689 (2018).
5. Lübken, F.-J., Baumgarten, G., Grygalashvyly, M. & Vellalassery, A. Absorption of solar radiation by noctilucent clouds in a changing climate. *Geophys. Res. Lett.* **51**, e2023GL107334 (2024).
6. Duft, D., Nachbar, M. & Leisner, T. Unravelling the microphysics of polar mesospheric cloud formation. *Atmos. Chem. Phys.* **19**, 2871e2879 (2019).
7. Saunders, R. W. & Plane, J. M. C. A photo-chemical method for the production of olivine nanoparticles as cosmic dust analogues. *Icarus* **212**, 373–382 (2011).
8. Gumbel, J. & Megner, L. Charged meteoric smoke as ice nuclei in the mesosphere: part 1: a review of basic concepts. *J. Atmos. Sol. Terr. Phys.* **71**, 1225–1235 (2009).
9. Gumbel, J. & Megner, L. Charged meteoric smoke as ice nuclei in the mesosphere: part 2: a feasibility study. *J. Atmos. Sol. Terr. Phys.* **71**, 1236–1244 (2009).
10. Hervig, M. E. et al. The content and composition of meteoric smoke in mesospheric ice particles from SOFIE observations. *J. Atmos. Sol. Terr. Phys.* **84-85**, 1–6 (2012).
11. Hedin, J. et al. The MAGIC meteoric smoke particle sampler. *J. Atmos. Sol. Terr. Phys.* **118**, 127–144 (2014).
12. Plane, J. M. C. Cosmic dust in the Earth's atmosphere. *Chem. Soc. Rev.* **41**, 6507–6518 (2012).
13. Carrillo-Sánchez, J. et al. Cosmic dust fluxes in the atmospheres of Earth, Mars, and Venus. *Icarus* **335**, 113395 (2020).
14. Plane, J. M. C., Feng, W. & Dawkins, E. C. M. The mesosphere and metals: chemistry and changes. *Chem. Rev.* **115**, 4497–4541 (2015).
15. Kalashnikova, O., Horanyi, M., Thomas, G. E. & Toon, O. B. Meteoric smoke production in the atmosphere. *Geophys. Res. Lett.* **27**, 3293–3296 (2000).

16. Hedin, J., Gumbel, J. & Rapp, M. On the efficiency of rocket-borne particle detection in the mesosphere. *Atm. Chem. Phys.* **7**, 3701–3711 (2007).
17. Arnyx, K. et al. In-situ measurement of smoke particles in the wintertime polar mesosphere between 80 and 85 km altitude. *J. Atmos. Sol. Terr. Phys.* **70**, 61–70 (2008).
18. Strelnikova, I., Rapp, M., Raizada, S. & Sulzer, M. Meteor smoke particle properties derived from Arecibo incoherent scatter radar observations. *Geophys. Res. Lett.* **34**, L15815 (2007).
19. Fentzke, J. T. et al. D region meteoric smoke and neutral temperature retrieval using the poker flat incoherent scatter radar. *Geophys. Res. Lett.* **39**, L21102 (2012).
20. Plane, J. M. C. et al. A combined rocket-borne and ground-based study of the sodium layer and charged dust in the upper mesosphere. *J. Atmos. Terr. Phys.* **118**, 151–160 (2014).
21. Molina-Cuberos, J. G., Lopez-Moreno, J. J. & Arnold, F. Meteoric layers in planetary atmospheres. *Space Sci. Rev.* **137**, 175–191 (2008).
22. Verronen, P. T., Andersson, M. E., Marsh, D. R., Kovács, T. & Plane, J. M. C. WACCM-D whole atmosphere community climate model with D-region ion chemistry. *J. Adv. Model. Earth Sy.* **8**, 954–975 (2016).
23. Gelinas, L. J. et al. Mesospheric charged dust layer: Implications for neutral chemistry. *J. Geophys. Res.* **110**, A01310 (2005).
24. Friedrich, M., Rapp, M., Plane, J. M. C. & Torkar, K. M. Bite-outs and other depletions of mesospheric electrons. *J. Atmos. Sol. Terr. Phys.* **73**, 2201–2211 (2011).
25. Friedrich, M. et al. Multi-instrument comparisons of D-region plasma measurements. *Ann. Geophys.* **31**, 135–144 (2013).
26. Skinner, L. M. & Sambles, J. R. The Kelvin equation–A review. *J. Aerosol Sci.* **3**, 199–210 (1972).
27. Summers, M. E. & Siskind, D. E. Surface recombination of O and H_2 on meteoric dust as a source of mesospheric water vapor. *Geophys. Res. Lett.* **26**, 1837–1840 (1999).
28. Guiu, J. M. et al. Cluster beam study of $(MgSiO_3)^+$-based monomeric silicate species and their interaction with oxygen: implications for interstellar astrochemistry. *ACS Earth Sp. Chem.* **6**, 2465–2470 (2022).
29. Escatllar, A. M., Lazaukas, T., Woodley, S. M. & Bromley, S. T. Structure and properties of nanosilicates with olivine $(Mg_2SiO_4)_N$ and pyroxene $(MgSiO_3)_N$ compositions. *ACS Earth Sp. Chem.* **3**, 2390–2403 (2019).
30. Kronik, L., Fromherz, R., Ko, E., Ganteför, G. & Chelikowsky J. R., Highest electron affinity as a predictor of cluster anion structures. *Nat. Mater.* **1**, 49–53 (2002).
31. Marom, N., Kim, M. & Chelikowsky, J. R. Structure selection based on high vertical electron affinity for TiO_2 clusters. *Phys. Rev. Lett.* **108**, 106801 (2012).
32. Lushchikova, O. V. et al. Structures of Cu_n^+ ($n = 3$–10) clusters obtained by infrared action spectroscopy. *J. Phys. Chem. Lett.* **10**, 2151–2155 (2019).
33. Gutowski, M., Skurski, P., Li, X. & Wang, L.-S. $(MgO)_n^-$ ($n = 1$–5) clusters: multipole-bound anions and photodetachment spectroscopy. *Phys. Rev. Lett.* **85**, 3145–3148 (2000).
34. Wang, L.-S., Wu, H., Desai, S. R., Fan, J. & Colson, S. D. A photoelectron spectroscopic study of small silicon oxide clusters: SiO_2, Si_2O_3, and Si_2O_4. *J. Phys. Chem.* **100**, 8697–8700 (1996).
35. Wang, L.-S., Nicholas, J. B., Dupuis, M., Wu, H. & Colson, S. D. Si_3O_y ($y = 1$–6) clusters: models for oxidation of silicon surfaces and defect sites in bulk oxide materials. *Phys. Rev. Lett.* **78**, 4450–4453 (1997).
36. Flikkema, E. & Bromley, S. T. Dedicated global optimization search for ground state silica nanoclusters: $(SiO_2)_N$ ($N = 6-12$). *J. Phys. Chem. B.* **108**, 9638–9645 (2004).
37. Escatllar, A. M. & Bromley, S. T. Assessing the viability of silicate nanoclusters as carriers of the anomalous microwave emission: a quantum mechanical study. *Astron. Astrophys.* **634**, A77 (2020).
38. Natanson, G. L. On the theory of the charging of microscopic aerosol particles as a result of capture of gas ions. *Sov. Phys. Tech. Phys.* **5**, 538–551 (1960).
39. Tobiska, W. K. et al. The SOLAR2000 empirical solar irradiance model and forecast tool. *J. Atmos. Sol. Terr. Phys.* **62**, 1233–1250 (2000).
40. Woo, S. B., Branscomb, L. M. & Beaty, E. C. Sunlight photodetachment rate of ground state O_2^-. *J. Geophys. Res.* **74**, 2933–2940 (1969).
41. Rapp, M. Rocket-borne in situ measurements of meteor smoke: charging properties and implications for seasonal variation. *J. Geophys. Res.* **115**, D00I16 (2010).
42. Fentzke, J. T., Janches, D., Strelnikova, I. & Rapp, M. Meteoric smoke particle properties derived using dual-beam Arecibo UHF observations of D-region spectra during different seasons. *J. Atmos. Sol. Terr. Phys.* **71**, 1982–1991 (2009).
43. Friedrich, M. et al. Electron loss and meteoric dust in the mesosphere. *Ann. Geophys.* **30**, 1495–1501 (2012).
44. Bakker, J. M. et al. Intensity-resolved IR multiple photon ionization and fragmentation of C_{60}. *J. Chem. Phys.* **132**, 074305 (2010).
45. Haertelt, M. et al. Structure determination of anionic metal clusters via infrared resonance-enhanced multiple photon electron detachment spectroscopy. *J. Phys. Chem. Lett.* **2**, 1720–1724 (2011).
46. Wales, D. J. & Doye, J. P. K. Global optimization by basin-hopping and the lowest energy structures of Lennard-Jones clusters containing up to 110 Atoms. *J. Phys. Chem. A.* **101**, 5111–5116 (1997).
47. Cuko, A., Macià, A., Calatayud, M. & Bromley, S. T. Global optimisation of hydroxylated silica clusters: A cascade Monte Carlo Basin Hopping approach. *Comput. Theor. Chem.* **1102**, 38–43 (2017).
48. Gale, J. D. GULP: a computer program for the symmetry-adapted simulation of solids. *J. Chem. Soc., Faraday Trans.* **93**, 629–637 (1997).
49. Bisbo, M. K. & Hammer, B. Efficient global structure optimization with a machine-learned surrogate model. *Phys. Rev. Lett.* **124**, 086102 (2020).
50. Adamo, C. & Barone, V. Toward reliable density functional methods without adjustable parameters: the PBE0 model. *J. Chem. Phys.* **110**, 6158–6170 (1999).
51. Blum, V. et al. Ab initio molecular simulations with numeric atom-centered orbitals. *Comput. Phys. Commun.* **180**, 2175–2196 (2009).
52. Jensen, S. R. et al. The elephant in the room of density functional theory calculations. *J. Phys. Chem. Lett.* **8**, 1449–1457 (2017).
53. Bhattacharya, S., Levchenko, S. V., Ghiringhelli, L. M. & Scheffler, M. Stability and metastability of clusters in a reactive atmosphere: theoretical evidence for unexpected stoichiometries of Mg_MO_x. *Phys. Rev. Lett.* **111**, 135501 (2013).
54. Tkatchenko, A. & Scheffler, M. Accurate molecular van der Waals interactions from ground-state electron density and free-atom reference data. *Phys. Rev. Lett.* **102**, 073005 (2009).
55. Guiu, J. M., Escatllar, A. M. & Bromley, S. T. How does temperature affect the infrared vibrational spectra of nanosized silicate dust? *ACS Earth Sp. Chem.* **5**, 812–823 (2021).
56. de la Pierre, M. et al. Performance of six functionals (LDA, PBE, PBESOL, B3LYP, PBE0, and WC1LYP) in the simulation of vibrational and dielectric properties of crystalline compounds. The case of forsterite Mg_2SiO_4. *J. Comput. Chem.* **32**, 1775–1784 (2011).
57. Demichelis, R. The infrared spectrum of ortho-enstatite from reflectance experiments and first principle simulations. *Mon. Not. R. Astron. Soc.* **420**, 147–154 (2012).
58. Perdew, P., Burke, K. & Ernzerhof, M. Generalized gradient approximation made simple. *Phys. Rev. Lett.* **77**, 3865–3868 (1996).
59. A comparison of DFT-calculated ozone frequencies using different functionals can be found at: https://cccbdb.nist.gov/.
60. de Avillez Pereira, R., Baulch, D. L., Pilling, M. J., Robertson, S. H. & Zeng, G. Temperature and pressure dependence of the multichannel rate coefficients for the $CH_3 + OH$ System. *J. Phys. Chem.* **101**, 9681–9693 (1997).

61. Troe, J., Miller, T. M. & Viggiano, A. A. Low-energy electron attachment to SF_6. I. Kinetic modeling of nondissociative attachment. *J. Chem. Phys.* **127**, 244303 (2007).
62. Su, T. & Chesnavich, W. J. Parametrization of the ion–polar molecule collision rate constant by trajectory calculations. *J. Chem. Phys.* **76**, 5183–5185 (1982).

Acknowledgements

S.M.L. gratefully acknowledges financial support from the Vector Stiftung (MINT Innovationen 2020) as well as Bianca-Andreea Ghejan for assistance in the data evaluation. We also thank the Nederlandse Organisatie voor Wetenschappelijk Onderzoek (NWO) for the support of the FELIX Laboratory. The research leading to these results has received funding from LASERLAB-EUROPE (grant agreement no. 654148, European Union's Horizon 2020 research and innovation program). J.M.C.P. was supported by the European Research Council (project number 291332 – CODITA). S.T.B. acknowledges support from the MICINN-funded PID2021-127957NB-I00 and TED2021-132550B-C21 project grants, and the Maria de Maeztu program for Spanish Structures of Excellence (CEX2021-001202-M) and project grant 2021SGR00354 funded by the Generalitat de Catalunya. J.M. acknowledges the Generalitat de Catalunya for the pre-doctoral grant 2020 FI-B-00617.

Author contributions

S.T.B. proposed the original concept for the study. S.M.L. performed all the cluster beam experiments and associated analysis. J.M.G. performed all the global optimisation searches, DFT calculations and associated analysis. J.M.C.P. performed the kinetic modelling and associated analysis and provided the discussion concerning the atmospheric relevance. S.M.L. and S.T.B. prepared the original version of the manuscript. All authors discussed the results of the study and contributed to revising the manuscript.

Competing interests

The authors declare no competing interests.

Additional information

Supplementary information The online version contains supplementary material available at https://doi.org/10.1038/s41612-025-01019-7.

Correspondence and requests for materials should be addressed to Stefan T. Bromley or Sandra M. Lang.

Reprints and permissions information is available at http://www.nature.com/reprints